Electrochimica Acta 316 (2019) 273–282

Contents lists available at ScienceDirect

Electrochimica Acta

journal homepage: www.elsevier.com/locate/electacta

Nucleation and growth kinetics of electrochemically deposited ceria nanostructures for high-temperature electrocatalysis

Yoonseok Choi [a], Jinwook Kim [a], Han Gil Seo [a], Harry L. Tuller [b], WooChul Jung [a, *]

[a] Department of Materials Science and Engineering, Korea Advanced Institute of Science and Technology (KAIST), 291 Daehak-ro, Yuseong-gu, Daejeon, 34141, Republic of Korea
[b] Department of Materials Science and Engineering, Massachusetts Institute of Technology (MIT), 77 Massachusetts Avenue, Cambridge, MA, 02139, USA

ARTICLE INFO

Article history:
Received 17 April 2019
Received in revised form
20 May 2019
Accepted 26 May 2019
Available online 27 May 2019

Keywords:
Electrochemical deposition
Nucleation and growth
Ceria (CeO_2)
Nanostructured thin film
Solid oxide fuel cell

ABSTRACT

Cathodic electrochemical deposition, a simple and cost-effective route for fabricating ceria nanostructures, has attracted much attention in catalysis and renewable energy technologies. However, electrochemical nucleation and growth mechanisms that determine the nanoscale architecture of ceria films during deposition have not yet been clarified. In this study, we analyze current and mass-time transients and thin film microstructures as functions of applied potential and temperature. We then examine these results in light of analytical models for the determination of relative nucleation rate, nuclei density, and diffusivity of Ce ion during ceria electrocrystallization. As applied potential and temperature decrease, the reduced deposition rate allows nuclei to branch, leading to more 'petal'-like nanostructures with high specific surface areas. These optimized ceria nanostructures greatly improve the hydrogen electro-oxidation rate and reduced electrode resistance when coated onto a model electrode that simulates a Ni/yttria-stabilized zirconia composite anode utilized in solid oxide fuel cells.

1. Introduction

Cathodic electrochemical deposition (CELD) has drawn considerable attention as an efficient fabrication method for metal-oxide thin films prepared from metal-salt precursor solutions [1–5]. This method is economical and advantageous for mass production given that it operates at room temperature and ambient pressure, with a simple apparatus and procedure. Furthermore, the composition, microstructure, and thickness of the coated films can be precisely controlled by changing easily accessible deposition parameters, including applied bias (or current density), temperature, and solution chemistry [6–10]. The typical CELD process consists of three steps: (1) electrogeneration of base, (2) chemical precipitation of metal hydroxides, and (3) oxide formation during the dehydration step, often including thermal treatments. Depending on the deposition potential, the solution pH, and the choice of precursors, the cathodic polarization electrochemically reduces chemical species such as O_2, NO_3^-, or H_2O (*e.g.* $NO_3^- + H_2O + 2e^- \rightarrow NO_2^- + 2OH^-$) in aqueous solution to form hydroxyl ions near the electrode surface. These reactions effectively compete with direct metal reduction ($M^{n+} + n^{e-} \rightarrow M^{(0)}$), and the generated OH^- ions induce precipitation of dissolved metal ions in the form of solid-state $M(OH)_n$, which, in turn, are transformed into an oxide during subsequent drying processes [6,11]. Metal oxides of various compositions, especially materials containing a reducible metal, can readily be synthesized by this method [6].

Among these potential materials, CeO_2 (ceria) is one of the most attractive due to its ubiquitous applications in catalysis and renewable energy technologies, such as catalysts for hydrocarbon reformers [12,13] and automobile exhaust systems [14–16], electrodes for high-temperature electrochemical cells [17–20], and oxygen carriers for solar-driven thermochemical reactors [21,22]. In the past decades, numerous ceria thin films prepared *via* electrochemical deposition have been reported [23–31], often doped with rare-earth elements [28,29,32–34] and 3d transition metals [35–37]. Considerable effort has been devoted to controlling the nanoscale architecture of ceria for use in (photo-)electrochemical or chemical catalysis. For example, Jung et al. showed that highly porous petal nanostructures of doped ceria with high specific surface area can dramatically enhance the reactivity toward H_2/CH_4 electro-oxidation of metal-based composite electrodes in solid oxide fuel cells (SOFCs) [5,38]. Also, Ma et al. reported improved photoelectrochemical performance of ceria nanobelts in

* Corresponding author.
E-mail address: wcjung@kaist.ac.kr (W. Jung).

https://doi.org/10.1016/j.electacta.2019.05.135
0013-4686/

photovoltaic applications [39], and Tong et al. reported excellent CO conversion activity with hierarchically porous ceria [26].

Nonetheless, little effort appears to have been directed toward understanding the growth kinetics of ceria nanostructures, critical for controlling microstructure with potential for producing further improvements in catalytic performance. Film surface morphologies often depend sensitively on the nucleation and growth processes involved in film growth, and in turn, on the deposition parameters utilized [40,41]. However, previous studies have focused either on the reaction pathways (*e.g.* the OH^- formation route or the precise point at which Ce^{3+} is oxidized to Ce^{4+}) [42,43], dopant effects [33,35], or additive effects [32,44,45]. To the best of our knowledge, information about nucleation and growth remains sparse. Li et al., using in-situ atomic force microscopy (AFM), found that initial electrochemical ceria formation proceeds from gel-like nuclei on the electrode surface; however, they paid more attention to microscopic crystallization processes [46,47]. Moreover, although Ringuedé et al. suggested that the variation of current with time during ceria thin film deposition could be related to the electrocrystallization growth process [47,48], neither in-depth electrochemical analysis nor correlation of that analysis with the final achieved film morphology was conducted.

The aim of this study is, therefore, to investigate the electrochemical nucleation and growth mechanisms of ceria on a metal, Ni in particular. Here, we precisely examine potentiostatic current density-time transients, and the corresponding deposited mass, utilizing a quartz crystal microbalance (QCM). The growth of ceria on Ni electrodes was determined to be dominated by the diffusion of Ce^{3+} ions within the experimental range of applied potential (−0.70 to −0.90 V vs. SCE) and temperature (RT to 55 °C). The classic analytical model for electrocrystallization enables extraction of the relative nucleation rate and nucleus density from the current density-time transient curves that vary with deposition conditions, thereby allowing us to understand the sources of the changes in surface morphology of the ceria films. We succeeded in achieving excellent electrochemical reactivity toward H_2 electro-oxidation by precisely tailoring structures of doped ceria thin films deposited onto patterned Ni/$(Y,Zr)O_2$ model SOFC anodes. These observations provide essential insights that enhance our understanding of the nucleation and growth behavior of electrochemically synthesized metal oxides and their possible technological applications.

2. Experimental

Electrochemical deposition was carried out in a standard three-electrode system combined with an electrochemical quartz crystal microbalances (INFICON Corp.). An AT-cut quartz crystal covered with Ni electrodes (5 MHz, MAXTEK Inc.) was used as the working electrode ($d = 1$ inch). The counter electrode was a platinum wire, and a saturated calomel electrode ((SCE, +0.241 V vs. SHE), Koslow) served as a reference electrode. The working electrode was cleaned by immersing it in 10 wt% nitric acid (HNO_3) for 20 s and then rinsing it with de-ionized (DI) water. Each electrode was carefully positioned while maintaining a constant distance from the other electrode and a constant depth in the solution. Solutions used in this study were prepared by dissolving cerium nitrate powders ($Ce(NO_3)_3 \cdot 6H_2O$, SAMCHUN, 99.99%) in 200 ml DI water (18.2 MΩ cm, 25 °C). 0.5M potassium chloride (KCl, KANTO, 99.9%) was used as the supporting electrolyte. The concentrations of dissolved oxygen gas were maintained at low levels by bubbling high purity N_2 for 1 hour (about 2.5 mg l^{-1}) through the solution before each deposition. The initial pH was adjusted to 3.3 ± 0.1 by the addition of 0.125 ml of 0.5 M hydrochloric acid (HCl). An external silicon oil bath was used to adjust the solution temperature to between 40 °C and 55 °C (Table S1). For simple and reliable electrochemical analysis, Ce^{3+} ion concentration and initial pH were fixed and the solution was deaerated to prevent the reduction of species other than NO_3^- (see Fig. S1).

Chronoamperometry (CA) and linear sweep voltammetry (LSV) (VSP-300, Biologic) were used to study the growth process associated with the electrochemical deposition of ceria films. To select the deposition potential range, linear sweep voltammetry was conducted with a scan rate of 20 mV s^{-1} (Fig. S1). For potentiostatic deposition, a cathodic potential ranging from −0.70 V to −0.90V vs. SCE was applied to study the nucleation and growth mechanisms. On the other hand, when investigating the effects of bath temperature, the potential was fixed at −0.80 V vs. SCE. To define the actual relative growth rates, potentiostatic deposition (in which the electric potential between the working electrode and reference electrode is controlled, while the current response from the counter electrode to the working electrode is measured) was terminated when a certain desired mass was achieved. Film properties were determined by scanning electron microscopy (SEM, Hitachi) and X-ray diffraction (XRD, Rigaku Ultima IV) using K_α(Cu) radiation (40 kV, 40 mA).

For electrochemical performance measurement, symmetrically patterned Ni/YSZ/patterned Ni anodes were fabricated. Using a photolithographic lift-off process, patterned Ni films were obtained on a (100) single crystal YSZ substrate (8 mol%, 10 × 10 × 0.5 mm, MTI Corp.). A positive photoresist (AZ5214) was spin-coated onto an YSZ substrate at 3000 rpm and baked at 115 °C for 1 min 30 s. After samples were aligned using a contact aligner (MDA-8000B, MIDAS Corp.), they were exposed to UV light for 12 s while in contact with a photomask. Next, the samples were immersed in developer for 35 s to obtain the photoresist patterns; this was followed by DI water rinsing, drying, and baking at 120 °C for 3 min in sequence. 300 nm-thick Ni films (99.99% target purity) were deposited by DC magnetron sputtering with a DC power of 100 W, a working pressure of 10 mTorr Ar, and a deposition rate of ~1 nm s^{-1}. Final Ni patterns were obtained by immersing the samples in acetone at room temperature with mild ultrasonication. The Ni stripe width and the Ni-to-Ni distance are both equal to 20 μm, with a corresponding Ni-YSZ-gas triple-phase boundary density of 324.8 cm cm^{-2} and exposed YSZ area of 0.32 cm^2 cm^{-2} (Fig. S2). Then, CELD was carried out on each side of the cell using the same apparatus and solution conditions, except for the addition of 5 mol % Sm ($Sm(NO_3)_3 \cdot 6H_2O$, 99.99%, Alfa Aesar) to the solution, to ensure sufficient ionic conductivity in the coating layers.

3. Results and discussion

3.1. Physical characterizations

Films were prepared in a potentiostatic mode with the total mass of the deposits kept constant. Fig. 1a–d are microscopic images showing how the shape of the electrochemically deposited ceria thin film changes with applied potential (−0.70 V to −0.90 V vs. SCE). Clearly, the applied potential has a significant influence on the morphology of the ceria films. The morphology of the ceria obtained at −0.70 V, in particular, shows nanoscale, sharp-edged 'petals', 10–50 nm in thickness (Fig. S3). On the other hand, as the magnitude of the applied potential increases, this unique nanoscale feature gradually attenuates to form a more planar, compact film. Noticeable cracks also begin to be observed at more negative potential, presumably due to larger induced internal stresses generated in the more compact films during drying/dehydration [49]. Fig. 1e shows typical XRD patterns of as-deposited ceria films after drying in air. All patterns display several diffraction peaks corresponding to the cubic fluorite structures of CeO_2, whereas no other possible cerium-rich phases

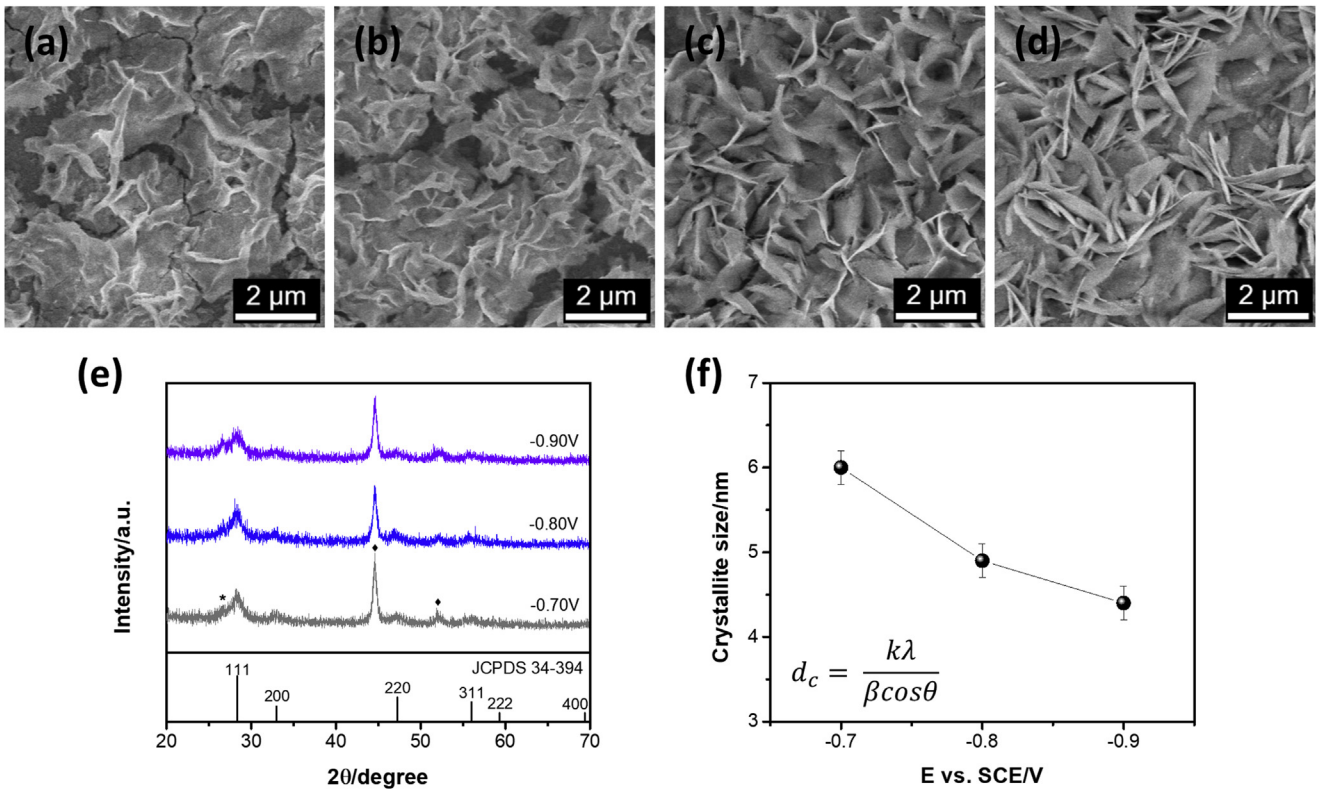

Fig. 1. Physical characterization of electrochemically fabricated ceria thin films. (a)–(d) The scanning electron microscope images of ceria thin films obtained by the application of (a) −0.90 V, (b) −0.80 V, (c) −0.75 V, (d) −0.70 V vs. SCE, respectively. (Deposit mass (m) is equal to 400 μg cm^{-2}) (e) The x-ray diffraction patterns obtained by applying −0.70 V (blue), −0.80 V (purple), −0.90 V (gray) vs. SCE. (*: residual KNO_3, ◆: Ni) (f) Crystallite size vs. applied potential, estimated according to the Scherrer equation [50]. (For interpretation of the references to colour in this figure legend, the reader is referred to the Web version of this article.)

such as $Ce(OH)_3$ or Ce_2O_3 are evident. These results show that crystallized ceria nanostructures can be readily obtained even at room temperature. As evidenced by the relatively broad peaks, the electrodeposits are largely nanocrystalline. These nanocrystalline features were additionally confirmed by SEM images taken at a higher magnification (Figs. S4a–c). We applied the Scherrer equation [50] to the (111) peaks of each sample to estimate the crystallite size associated with applied potential; the results are shown in Fig. 1f. The crystallite size is observed to remain at < 6 nm; decreasing from 6.0 ± 0.2 nm at −0.70 V to 4.5 ± 0.2 nm at −0.90 V. Decreasing crystallite size with applied potential occurs mainly when nucleation is more favorable than growth, in good agreement with previous studies [43]. Thus, the potential applied to the working electrode appears to drive nucleation that serves to reduce the nuclei size, while impeding the formation of branched nanostructures.

3.2. Electrochemical characterizations

Typical current density (j) and mass (m) transients resulting from potentiostatic deposition with three different potential values of −0.70 V, −0.80 V, and −0.90 V vs. SCE are shown in Fig. 2a–c. When a negative potential is applied, each of the two curves (j & m) can be divided into two regions after the initial rapid double-layer charging. The first region (region I) is the one in which no noticeable mass change is measured while cathodic current flows (See dashed line in insets). In the second region (region II), j increases to its maximum (j_m). Following that, the current decays, closely approaching a $t^{-1/2}$ decrease (except for the −0.70 V case due to the too-slow deposition rate in our measurement conditions), while the deposited mass keeps increasing. Here, we would like to highlight three important points. First, region I reflects the incubation time needed to reach a sufficient pH for $Ce(OH)_3$ precipitation, as suggested by Pedraza et al. [51], and thus corresponds to the step of base electrogeneration. This also means that the next region is attributed to the formation and growth of nuclei. Second, the relative evolution of the current density over time remains similar in all samples regardless of applied potential. A more negative potential shortens the deposition time for each region, while increasing the current density, but the shapes of all curves in Fig. 2a–c are similar, which implies that they share the same nucleation and growth mechanism [51,52]. In contrast, such evolution of the current density, independent of potential, cannot be observed when multiple mechanisms take place consecutively during electrodeposition, as proposed in the literature [41,53]. Third, the current response, after j_m decreases with its dependence on $t^{-1/2}$, as described by the Cottrell equation [54], is established when the overall reaction rate is determined by mass transfer of metal ions supplied during a typical metal electrodeposition. Accordingly, it is concluded that the electrogeneration of OH^- ions is facile enough to readily produce $Ce(OH)_3$ and the overall process, under the experimental conditions used in this study, is governed by Ce^{3+} diffusion to the near-electrode surface. Note that a film grows continuously without a quick drop in deposition rate, indicating the formation of a porous film. This result suggests that the deposition of ceria (or $Ce(OH)_3$) takes place more favorably onto the ceria as opposed to the Ni surface. This may be due to the difference in surface energy between the ceria deposits and the Ni metal, and

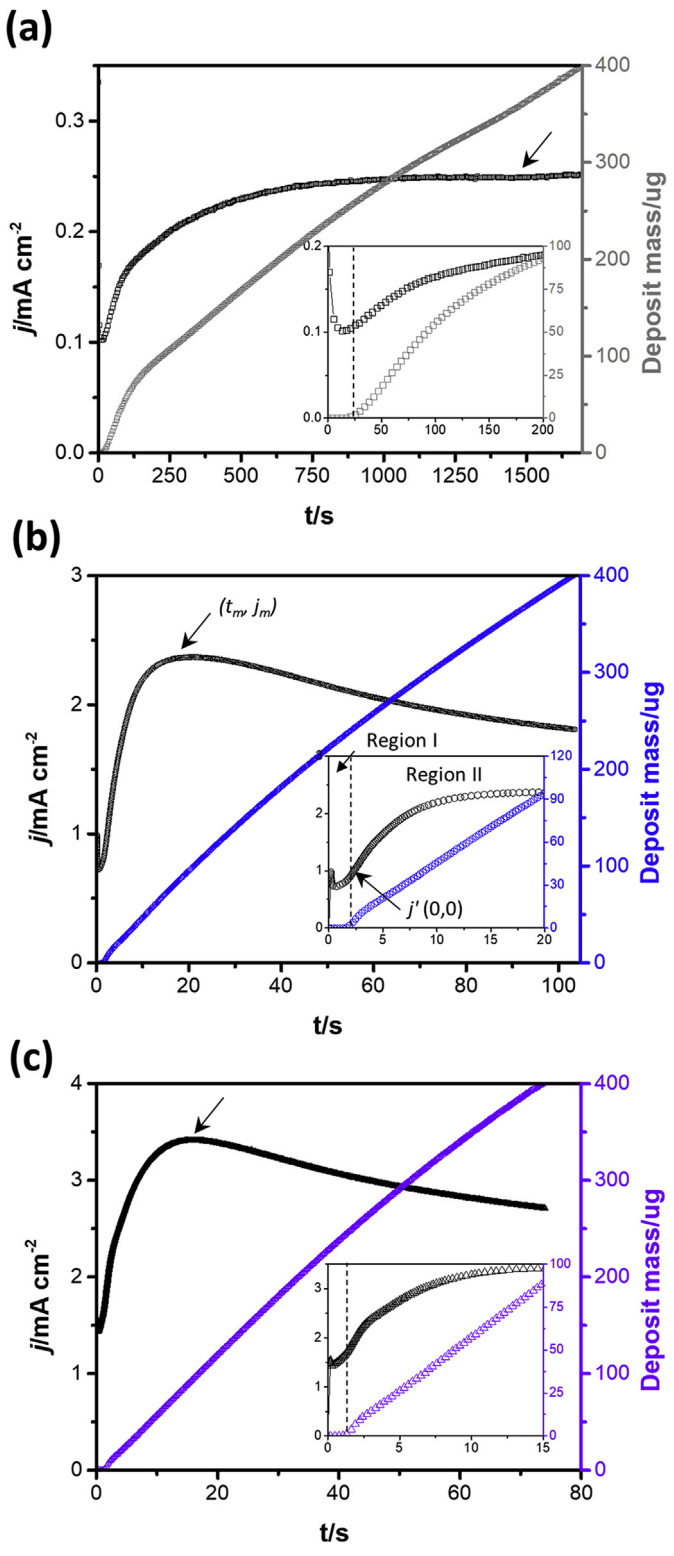

Fig. 2. Electrochemical characterizations of ceria CELD. (a)–(c) Double y-axes plot of potentiostatic current density-time transients (left y-axis) and mass-time transients (right y-axis) for CeO_2 CELD onto Ni substrates by the application of −0.70 V, −0.80 V, and −0.90 V vs. SCE, respectively. (inset: magnified plot for the initial CELD stage).

further study is needed to understand this phenomenon more fully.

3.3. Nucleation and growth mechanism

Since the electrogenerated OH^- ions are consumed by subsequent precipitation of $Ce(OH)_3$, the current response during the deposition process reflects the kinetics of the ensuing chemical reactions, which involve nucleation and growth in solution [54]. To examine the reaction kinetics in depth, we analyzed the current-time transient curves using theoretical models that describe 3D nucleation with diffusion-controlled growth [55,56]. Scharifker and Hills proposed kinetic models that can be divided into two limiting cases; 'instantaneous nucleation ($(3D\text{-}IN)_{diff.}$)' and 'progressive nucleation ($(3D\text{-}PN)_{diff.}$)' [56]. 'Instantaneous' means that the maximum number of nuclei is formed immediately after applying the potential at a fast rate. In contrast, 'progressive' indicates that fresh nuclei are formed continuously at a slow rate. Also, they provided a dimensionless diagnostic plot of $(j/j_m)^2$ vs. t/t_m, which allows one to determine whether the formation of the nuclei is instantaneous or progressive (Equations (1) and (2)). j_m and t_m correspond to the peak in the current density and time coordinates.

$$(3D-IN)_{diff.}: \left(\frac{i}{i_m}\right)^2 = \frac{1.9542}{\left(\frac{t}{t_m}\right)}\left\{1-\exp\left[-1.2564\left(\frac{t}{t_m}\right)\right]\right\}^2 \quad (1)$$

$$(3D-PN)_{diff.}: \left(\frac{i}{i_m}\right)^2 = \frac{1.2254}{\left(\frac{t}{t_m}\right)}\left\{1-\exp\left[-2.3367\left(\frac{t}{t_m}\right)^2\right]\right\}^2 \quad (2)$$

In Fig. 3a, it can be clearly seen that the experimental result agrees well with the case of instantaneous nucleation. It is noteworthy that the model used in this study basically describes the electroplating process and does not consider the electrogeneration step (region I) of the base. Thus, we set the point at which the mass starts to increase after the electrode potential is applied as a new offset origin ($j'(0,0)$ in the inset of Fig. 2b). This allows a precise analysis of the current variation solely associated with the electrochemical nucleation and growth process [36]. Then, the experimental data were fit using the theoretical current density-time transient equations corresponding to the $(3D\text{-}IN)_{diff.}$ case (Equation (3)).

$$j(t) = \frac{C_1}{\sqrt{t}}[1-\exp(-C_2 t)] \quad (3)$$

$C_1 = zFD^{1/2}c\pi^{-1/2}$ and $C_2 = N\pi D(8\pi cM)^{1/2}\rho^{-1/2}$ are constants in which zF is the molar charge, D the diffusion coefficient, and c the bulk concentration; M and ρ are the molar weight and density of deposits, respectively, and N is the total number of nuclei. The specific values for $Ce(OH)_3$ are listed in Table S2. It was confirmed that the single theoretical model fits with the experimental data well, in which R-square values typically range from 0.9908 to 0.9992 (Fig. 3b).

The values of C_1 and C_2 obtained from the fitting results as a function of applied potential are summarized in Fig. 4a. As denoted in the equation, the C_1 values are related to the diffusion coefficient (D) of the cations, which turns out to be almost independent of applied potential. The averaged diffusion coefficient is $(1.3 \pm 0.4) \times 10^{-6}$ cm^2 s^{-1}, is similar in magnitude to the previously reported D of Ce^{3+} in aqueous solution, 4.1×10^{-6} cm^2 s^{-1} at 20 °C, determined by the capillary cell method [57]. In contrast, C_2 values reflecting the number of nuclei (N), substantially increase up to one order of magnitude from −0.70 V to −0.90 V vs. SCE. This clearly indicates that the applied potential drives the nucleation process to

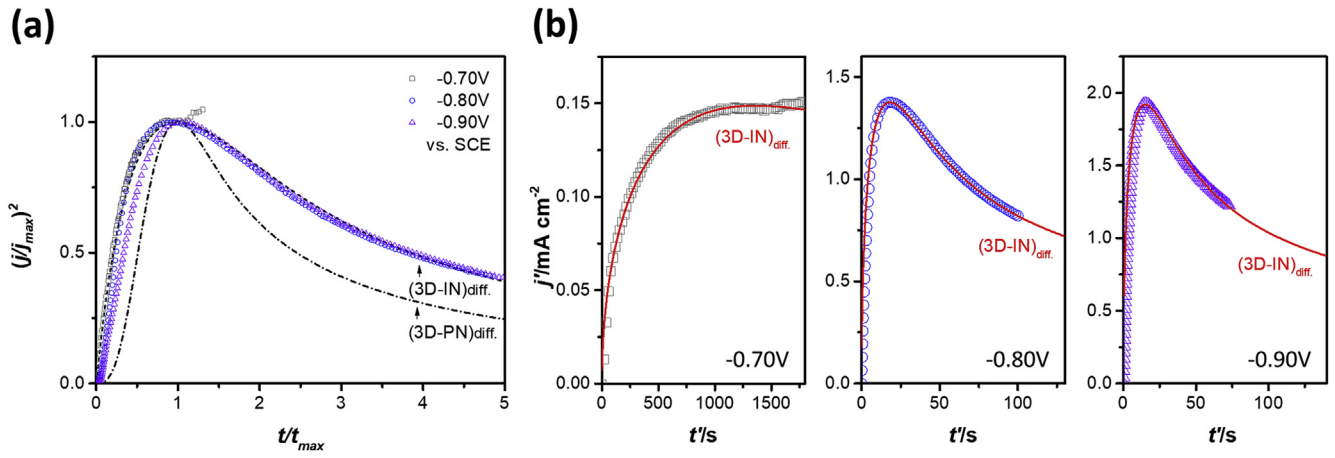

Fig. 3. Comparison of the experimental *j-t* curves to the theoretical models. (a) Theoretical non-dimensional diagnostic plots $((j/j_{max})^2$ vs. $t/t_{max})$ for respective instantaneous (3D-IN, dash line) and progressive (3D-PN, dash-dot line) nucleation and growth model controlled by diffusion and the experimental results of j-t curves in Fig. 2a–c. (b) Fitting results with Equation (3) corresponding to the 3D diffusion-limited instantaneous nucleation and growth mechanism (Red solid lines) for −0.70 V, −0.80 V, and −0.90 V vs. SCE., respectively. The potentiostatic current density-time transient curves were corrected according to the new origin *j'*(0, 0) indicated in Fig. 2b where actual nucleation begins. (For interpretation of the references to colour in this figure legend, the reader is referred to the Web version of this article.)

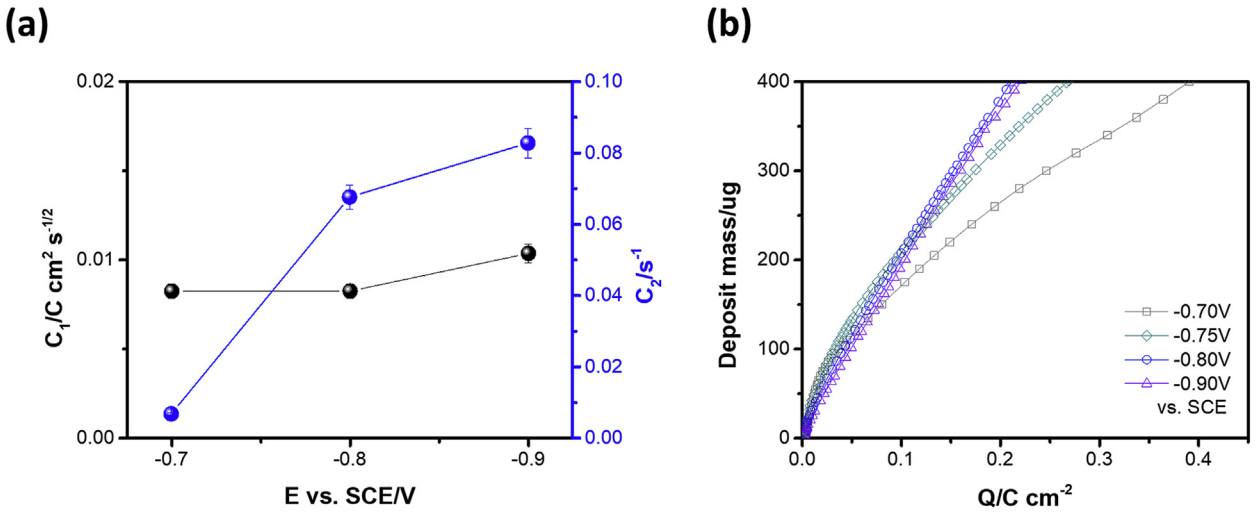

Fig. 4. Kinetic information from fitting and efficiency comparison with different cathodic potential. (a) Kinetic parameters (C_1 and C_2) obtained by fitting the current density-time transient curves with Equation (3). (b) Deposit mass (m) vs. charge density (Q) curves for CeO_2 CELD by the application of −0.70 V, −0.80 V, and −0.90 V vs. SCE, respectively.

accelerate [40,58] with estimated N values of $7.8 \times 10^3\ cm^{-2}$ and $9.4 \times 10^4\ cm^{-2}$ respectively. In the case of instantaneous nuclei formation, the increased number of nuclei leads to decreased nuclei diameters because the formation of an individual nucleus is restricted by adjacent nuclei. Accordingly, this result demonstrates that the observed decreasing crystallite size at higher negative potential, seen in Fig. 1f, is consistent with this mechanism.

Fig. 4b presents a graph of measured deposit mass (m) vs. charge density (Q). After an initial period in which parabolic variation is observed, probably due to the nucleation step [59], the curve is nearly linear, with slopes of $0.70\ mg\ C^{-1}$ (−0.70 V), $1.82\ mg\ C^{-1}$ (−0.80 V), and $1.80\ mg\ C^{-1}$ (−0.90 V). In general, the slope, corresponding to the efficiency of the deposition process, is theoretically estimated by the direct proportionality between the Faradaic current density and the electrochemical reaction rate (Faraday's law). However, interestingly, for the ceria CELD, the slope gradually increases with applied potential from −0.70 V to −0.80 V, and then saturates. For ceria CELD, although Faradaic efficiency is maintained during the electrochemical reduction of NO_3^- ions (or $n_{OH^-}/n_{e^-} = 1$), the yields of ceria on the electrode surface can be different because the chemical precipitation of $Ce(OH)_3$ is dependent on pH. At more negative potential, the increased reduction rate of nitrate ions yields higher pH near the electrode surface, which tends to stabilize hydroxide precipitates. Also, the lack of further increase in efficiency at potential less than −0.80 V implies theoretically limited efficiency or pH saturation caused by the reduction limiting current of NO_3^- [60]. Therefore, given the coincidental trend of the nucleation rate and deposition efficiency according to the applied potential (Fig. 4a and b), it can be concluded that the potential-dependent pH at the working electrodes determines the overall kinetics of deposition.

In Fig. 5, the effects of applied potential on the size, density of nuclei and the ensuing morphology of the thin films is schematically presented with the corresponding subsequent current-time transients. In the early stages of electrical generation of the base, the pH gradient of the solution formed near the electrode surface conversely induces a Ce^{3+} depletion region as the instantaneous nucleation occurs. As a result, metal ions diffuse from the bulk

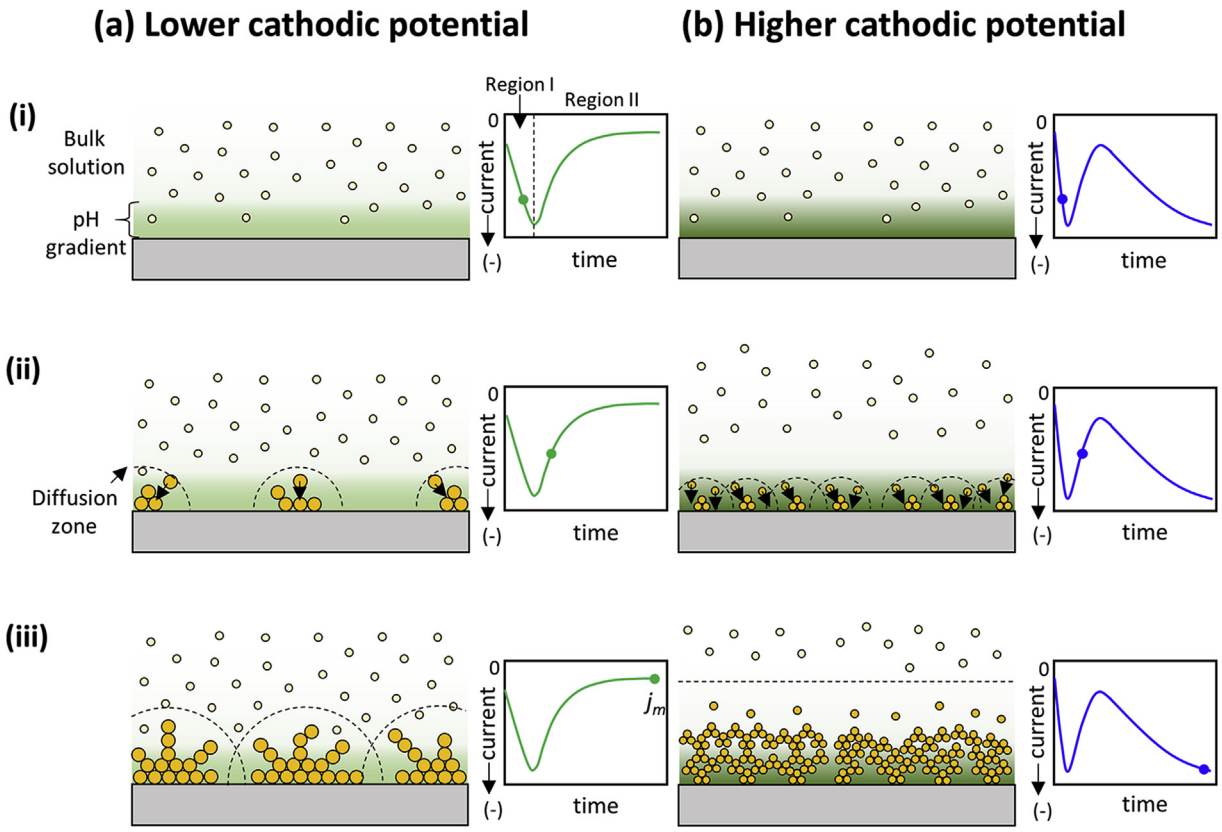

Fig. 5. Schematic presentation of the CeO_2 nucleation and growth at various stages of potentiostatic CELD. (a) lower magnitude of cathodic potential and (b) higher magnitude of cathodic potential. Depicted stages are (i) electro-generation of base, (ii) instantaneous nucleation, and (iii) planar diffusion-limited growth. The pH levels are shown as the pH is high enough to produce cerium hydroxides, inducing the depletion region of Ce^{3+} cations.

solution to the electrodes through the diffusion zone as described by the diffusion-limited growth model [56]; however, in the case of CELD, the formation of nuclei and their growth can take place in the solution above the electrode surface where the pH is high enough to precipitate $Ce(OH)_3$. In the case of lower pH induced by less negative potential (Fig. 5a), the driving force for nucleation is slow, resulting in smaller density of nuclei with larger sizes. This condition allows the nuclei to deposit on energetically more preferential sites and form distinctive nanostructures. On the other hand, a faster growth rate reduces this effect, resulting in more random precipitation on the crystal (Fig. 5b).

3.4. Temperature effect

Temperature is a key parameter that controls the growth rate of electrochemical deposition. We also investigated the effect of temperature on the process kinetics and resulting ceria morphology [9,58]. The variations of current density (j) and mass (m) as a function of time for different bath temperatures in the range of 23–55 °C for bulk concentration of 0.05 M under applied potential of −0.80 V vs. SCE are shown in Fig. 6a. It is obvious that the overall deposition rate increases with increasing temperature because the same amount of deposit is obtained in reduced time. On the other hand, the diagnostic plot in Fig. 6b shows that the instantaneous nucleation process, controlled by diffusion, still holds for all conditions; hence, the same theoretical model as that in the previous section can be used to study the detailed growth processes. Fig. 6c summarizes the C_1 and C_2 values derived from the fitting results (Fig. S5). These results show that both the diffusion coefficient (D) and the number of nuclei (N) increase with temperature. Using the calculated diffusion coefficients (D), an activation energy (E_A) of 0.20 eV is obtained, close to the previously reported value of 0.22 eV [57]. Also, the density of nuclei (N) increased with temperature. As a result, it was found that the nanoscale morphology was further attenuated at elevated temperature, as shown in Fig. 7 (see also Fig. 1b). However, unlike the increase of the applied potential, increasing temperature results in larger crystallites, 46.2 ± 0.1 nm (T = 55 °C) (Fig. S6 & Fig. S4e). We attribute this result to the promotion of hydrolysis, crystallization, and coagulation. These can additionally contribute to the more compact structure of the film at 55 °C. Also, the process efficiency is found to be almost independent of deposition temperature (Fig. 6d) [49], suggesting a saturation of pH near the working electrodes. Overall, it can be concluded that higher driving force tends to produce less-nanostructured ceria thin films.

3.5. Electrochemical performance

Since the discussion so far has demonstrated that it is possible to fabricate ceria nanostructures in a controlled fashion, we next examined how the shape control affects catalytic properties. The hydrogen electro-oxidation reaction was selected as the target reaction. Ceria is known to be an excellent oxygen ion solid electrolyte when doped with a lower valent cation, with best results obtained with either Sm or Gd [61]. In this study, Sm was selected as the dopant for ceria. To quantitatively analyze the morphology effect on catalytic activity, Sm-doped CeO_2 (SDC) was electrochemically deposited as a function of applied potential on geometrically well-defined Ni/YSZ electrodes with the same density of Ni-YSZ-gas triple phase boundaries (d_{3PB}) and Ni surface area

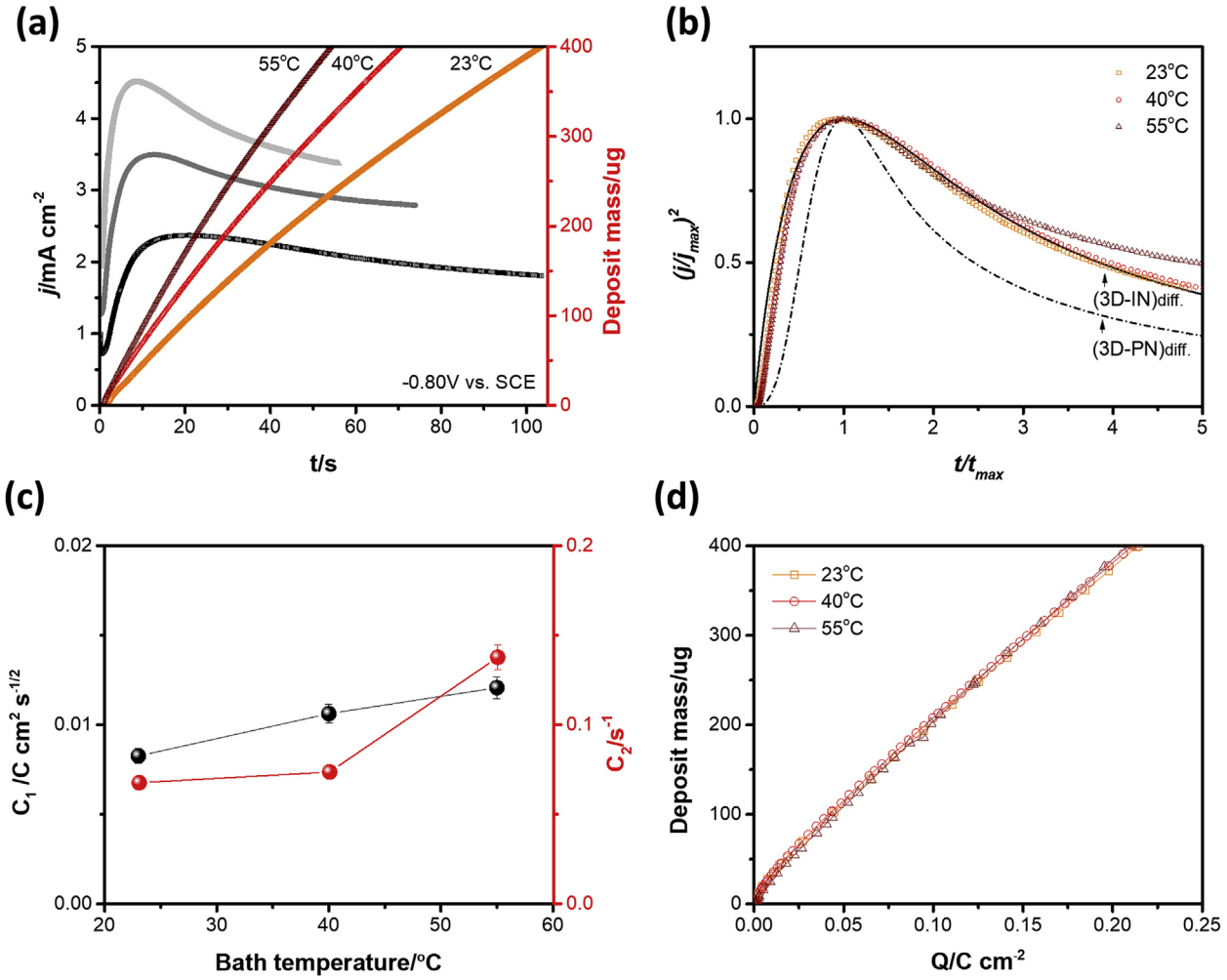

Fig. 6. Temperature effects on the ceria CELD. (a) Double y-axes plot of potentiostatic current density-time transients (left y-axis) and mass-time transients (right y-axis) for CeO_2 CELD onto Ni substrates by the application of −0.80 V vs. SCE at room temperature, 40 °C, and 55 °C, respectively. (b) Theoretical non-dimensional diagnostic plots $((j/j_{max})^2$ vs. $t/t_{max})$ for respective instantaneous (3D-IN, dash line) and progressive (3D-PN, dash-dot line) nucleation and growth model controlled by diffusion with the experimental results in Fig. 6a. (c) Kinetic parameters (C_1 and C_2) obtained by fitting the current density-time transient curves with Equation (3). (d) Corresponding deposit mass (m) vs. charge density (Q) curves.

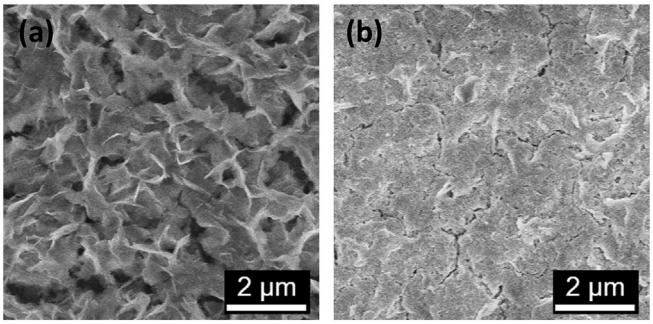

Fig. 7. SEM images of the electrochemically deposited ceria thin films with different deposition temperature. (a) $T_{bath} = 40$ °C and (b) $T_{bath} = 55$ °C when the deposit mass (m) is equal to 400 μg cm^{-2} (−0.80V vs. SCE) (see Fig. 1b obtained at room temperature for comparison).

(A_{Ni}) [5,38,62]. We selected two different applied potentials −0.65 V and −0.90 V vs. SCE that produced substantially different morphologies. Considering the previous observations that the Sm dopant tends to make the films less nanostructured [38,48], we used an applied potential of −0.65 V to obtain a nanostructured type of morphology similar to that obtained at −0.70 V for pure ceria. By using EDS analysis, we found that 19 at% (−0.65V) and 13 at% (−0.90 V) Sm was doped in the final films in 5 mol% Sm-containing solutions. The electrocatalytic activity of coated Ni-YSZ electrodes, as part of symmetric Ni-YSZ/YSZ/Ni-YSZ electrochemical cells, was analyzed by AC impedance spectroscopy (ACIS). Here, we note that the previously described shape change of the coating layers with applied potential is maintained despite Sm doping (Fig. S7).

Fig. 8a and b shows the typical impedance spectra of bare Ni/YSZ and CELD coated Ni/YSZ with different Sm-doped ceria (SDC) morphology (Figs. S7a and S7d), obtained under the conditions of wet H_2 atmosphere (10% H_2/1.3% H_2O) at 650 °C. All impedance spectra exhibit an offset resistance (R_{offset}), which remains nearly identical regardless of the presence of the SDC coating. This term corresponds to the sum of the YSZ electrolyte resistance and the sheet resistance of the Ni current collectors, and the average R_{offset}, 25.3 ± 3.3 Ω, is in good agreement with that estimated with data from the literature on the ionic conductivity of YSZ and the electrical conductivity of Ni at 650 °C [63,64]. For ease of comparison, R_{offset} was subtracted. Compared to a single arc in the impedance

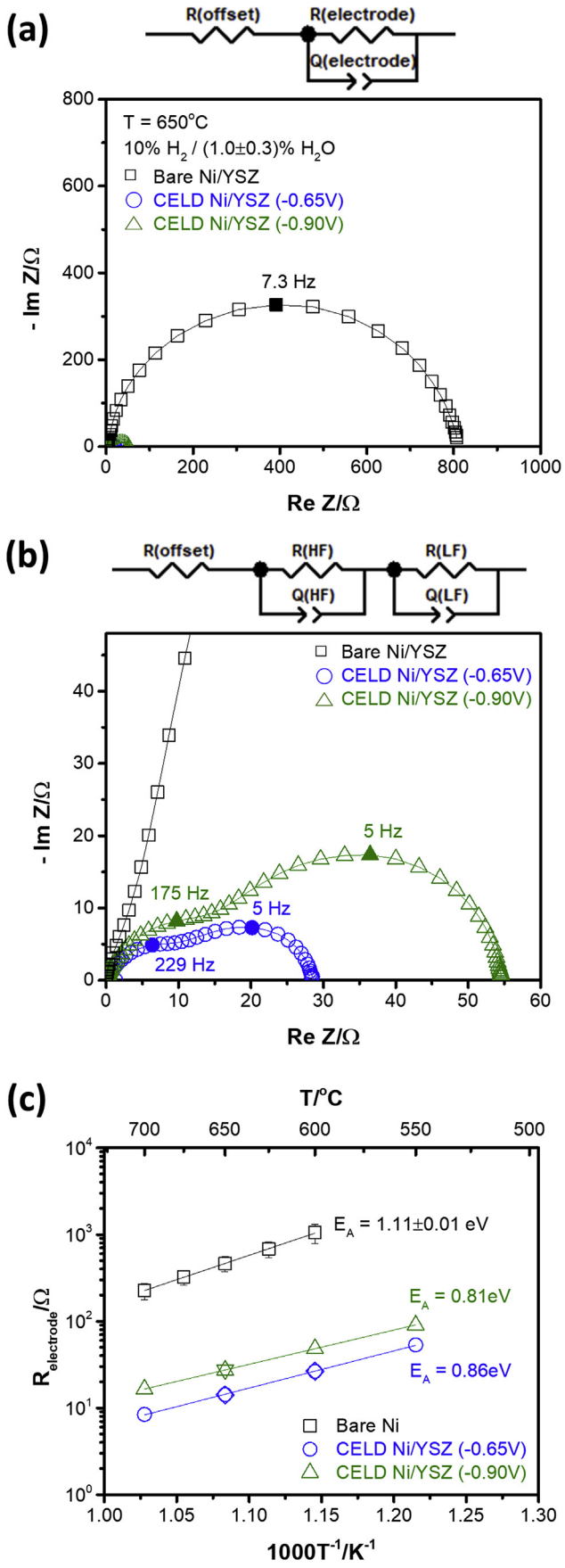

spectra of Ni/YSZ (Fig. 8a), the responses from the CELD coated Ni/YSZ electrodes consist of two serial arcs of $R_{HF}Q_{HF}$-$R_{LF}Q_{LF}$, where Q is a constant-phase element (Fig. 8b). The extracted C_{LF} values using $C = (R^{1-n}Q)^{1/n}$ are much larger than the C_{HF} values, 2.55 ± 0.99 mF vs. 0.14 ± 0.02 mF, and C_{LF} shows a pO_2-dependence with a slope of ~1/4 in the double logarithmic plot (Fig. S8). These results indicate that there is a chemical capacitance associated with the deposited ceria [38,65]. As in previous studies, while the arc in the low frequency region was revealed to stem from the characteristics of the ceria/gas interfaces [38], the origin of the arc in the high frequency region is not yet fully understood [45,66]. In this regard, to avoid the uncertainty, we rather use the sum of the arcs ($R_{HF} + R_{LF}$) as the electrode resistance ($R_{electrode}$). Importantly, one observes that the SDC coatings dramatically reduce the electrode resistance when compared to bare Ni/YSZ. For these specific examples, the reductions in electrode resistance amount to a factor of 1/18 (−0.65 V) and 1/10 (−0.90 V) compared to the bare electrode value. The enhancement in electrode performance for the SDC coated electrodes is more pronounced at lower temperature due to the lower apparent activation energy of $R_{electrode}$ for the coated electrodes, *i.e.* 1.07 eV vs 0.84 ± 0.03 eV, as shown in Fig. 8c. This observation is very interesting considering that it is obtained with only a few minutes of coating at room temperature without additional heat treatment, given that simple drying following deposition causes sufficient ceria crystallization, as noted in the previous XRD results (Fig. 1e). In addition, more crystalline films were obtained according to the measurements, as evidenced by the XRD results following the impedance measurements, which showed that the crystallite sizes of the −0.65 V and −0.90 V samples increased to 17.2 nm and 18.9 nm, respectively (Fig. S9). We note that these changes did not result in any change in resistance during heating and cooling during the measurement (Figs. 8c and S9), which suggests not only that crystallite growth can occur rapidly due to the thermal energy involved in the initial heating step to 700 °C but also that the film has high morphological stability. It should further be noted that the impedance is indeed dependent on ceria morphology, as evidenced by the reduced value of $R_{electrode}$ with the more-nanostructured ceria thin film. Under the reducing conditions associated with the H_2 atmosphere at high temperatures, doped ceria offers mixed ionic and electronic conductivity (MIEC) and has an inherently high activity for H_2 electro-oxidation, such that the reaction dominantly occurs on the oxide surface, with minimal contribution from the oxide-metal-gas boundaries (3 PBs) [18,38,67]. Therefore, given the unconventional electrochemical reaction pathway on the SDC surface, we attribute the remarkably enhanced reactivity of CELD-coated Ni/YSZ, and the higher reactivity of the more-nanostructured SDC layers obtained at −0.65 V, mainly to the increased density of reaction sites, *i.e.* to the specific surface area of the SDC coating layer. Our results demonstrate that straight-forward control of applied electrode potential or other readily accessible process parameters such as temperature are highly useful in optimizing the catalytic activity of structures prepared by cathodic electrochemical deposition.

Fig. 8. High-temperature electrochemical activity of CELD-SDC coated Ni/YSZ model electrodes. (a) Typical impedance spectra of Bare Ni/YSZ (black □), and CELD coated Ni/YSZ with different SDC film morphologies obtained by the application of −0.65 V (blue ○) and −0.90 V (green △) vs. SCE under wet H_2 (10%H_2/1.0 ± 0.3% H_2O, N_2 balanced). (b) Magnified plot of Fig. 8a for comparison between CELD coated samples with different applied potentials. (c) Temperature dependence of electrode resistance in Arrhenius plot of Bare Ni/YSZ (black □), and CELD coated Ni/YSZ of −0.65 V (blue ○) and −0.90 V (green △) vs. SCE under wet H_2 (10%H_2/1.3% H_2O, N_2 balanced). Here, the symbols ▽ and ◇ show the data obtained during heating and cooling steps. (For interpretation of the references to colour in this figure legend, the reader is referred to the Web version of this article.)

4. Conclusions

Through combined chronoamperometry and electrochemical quartz crystal microbalance techniques, we successfully elucidated the nucleation and growth mechanisms of ceria thin films electrochemically deposited onto nickel-YSZ electrodes, providing a holistic picture of the two-step deposition pathway involving (i) electrogeneration of base and (ii) hydroxide precipitation. The current-time transient curves were precisely investigated by applying classical electrochemical nucleation and diffusion-controlled growth theory. Excellent agreement of experimental data with predictions for instantaneous formation of nuclei was found for electrochemical deposition of ceria in the potential range −0.70 to −0.90 V vs. SCE and temperature range of 23–55 °C.

Both applied potential and temperature had profound influences on the kinetics of the nucleation and growth process. In case of applied potential, an increase in magnitude resulted in a faster deposition rate, and correspondingly, nuclei with smaller size and higher population density. This can be attributed to the increased solution pH near the Ni-YSZ surface, supported by the potential-dependent process efficiency. On the other hand, an increase in temperature produced nuclei with larger and higher population density, without significant change in efficiency and with an even further-increased deposition rate. These findings allowed us to elucidate the final surface morphology. The conditions of slower deposition rate, *i.e.* lower magnitude of applied potential, or lower deposition temperature, allow nuclei to branch, resulting in 'petal' nanostructures, despite the increased deposition time. On the contrary, the opposite conditions cause the nuclei to be randomly deposited in a short time on the electrode surface, restraining branching.

Finally, the impact of electrochemically prepared SDC with different morphologies on electrode activity was analyzed. Although the impact of electrochemically coated SDC in reducing the electrode resistance of patterned Ni/YSZ model anodes toward H_2 electrooxidation at high temperature is remarkable, we clearly observed that the nanoscale-architectured ceria layer, with higher specific surface area, shows even lower electrode resistance. Our study provides fundamental criteria for the selection of process parameters for the electrochemical coating method that can be applied to design highly effective catalytic structures.

Acknowledgements

This work was supported by the Korea Institute of Energy Technology Evaluation and Planning, the Ministry of Trade, Industry and Energy of the Republic of Korea (No. 20163030031850 and No. 20174030201590) and the U.S. Department of Energy, Office of Basic Science under grant DE SC0002633.

Appendix A. Supplementary data

Supplementary data to this article can be found online at https://doi.org/10.1016/j.electacta.2019.05.135.

References

[1] J. Elias, C. Levy-Clement, M. Bechelany, J. Michler, G.-Y. Wang, Z. Wang, L. Philippe, Adv. Mater. 22 (14) (2010) 1607.
[2] T. Zhai, S.L. Xie, M.H. Yu, P.P. Fang, C.L. Liang, X.H. Lu, Y.X. Tong, Nanomater. Energy 8 (2014) 255–263.
[3] Y.B. Zhang, B. Wang, F. Liu, J.P. Cheng, X.W. Zhang, L. Zhang, Nanomater. Energy 27 (2016) 627–637.
[4] W.J. Liu, H.B. Ge, Z.W. Gu, X.L. Lu, J.X. Li, J. Wang, Small 14 (45) (2018).
[5] H.G. Seo, Y. Choi, W. Jung, Adv. Energy Mater. 8 (19) (2018) 1303647.
[6] G.H.A. Therese, P.V. Kamath, Chem. Mater. 12 (5) (2000) 1195–1204.
[7] I. Zhitomirsky, Adv. Colloid Interfac. 97 (1–3) (2002) 279–317.
[8] K.S. Choi, Dalton Trans. 40 (2008) 5432–5438.
[9] T. Pauporte, E. Jouanno, F. Pelle, B. Viana, P. Aschehoug, J. Phys. Chem. C 113 (24) (2009) 10422–10431.
[10] Y. Wu, S.B. Sang, W.J. Zhong, F. Li, K.Y. Liu, H.T. Liu, Z.G. Lu, Q.M. Wu, Electrochim. Acta 261 (2018) 58–65.
[11] M. Pourbaix, Atlas of Electrochemical Equlibria in Aqueous Solutions, First English ed., Pergamon Press Ltd, 1966.
[12] Q. Fu, H. Saltsburg, M. Flytzani-Stephanopoulos, Science 301 (5635) (2003) 935–938.
[13] R. Si, M. Flytzani-Stephanopoulos, Angew. Chem. Int. Ed. 47 (15) (2008) 2884–2887.
[14] J. Kaspar, P. Fornasiero, M. Graziani, Catal. Today 50 (2) (1999) 285–298.
[15] M. Boaro, M. Vicario, C. de Leitenburg, G. Dolcetti, A. Trovarelli, Catal. Today 77 (4) (2003) 407–417.
[16] S. Lee, J. Seo, W. Jung, Nanoscale 8 (19) (2016) 10219–10228.
[17] E.P. Murray, T. Tsai, S.A. Barnett, Nature 400 (6745) (1999) 649–651.
[18] W. Jung, J.O. Dereux, W.C. Chueh, Y. Hao, S.M. Haile, Energy Environ. Sci. 5 (9) (2012) 8682–8689.
[19] W. Jung, K.L. Gu, Y. Choi, S.M. Haile, Energy Environ. Sci. 7 (5) (2014) 1685–1692.
[20] G.M. Yang, C. Su, Y.B. Chen, M.O. Tade, Z.P. Shao, J. Mater. Chem. 2 (45) (2014) 19526–19535.
[21] W.C. Chueh, C. Falter, M. Abbott, D. Scipio, P. Furler, S.M. Haile, A. Steinfeld, Science 330 (6012) (2010) 1797–1801.
[22] P. Furler, J.R. Scheffe, A. Steinfeld, Energy Environ. Sci. 5 (3) (2012) 6098–6103.
[23] R. Inguanta, S. Piazza, C. Sunseri, Nanotechnology 18 (48) (2007) 485605.
[24] G.R. Li, D.L. Qu, X.L. Yu, Y.X. Tong, Langmuir 24 (8) (2008) 4254–4259.
[25] P. Bocchetta, M. Santamaria, F. Di Quarto, J. Appl. Electrochem. 39 (11) (2009) 2073–2081.
[26] G.R. Li, D.L. Qu, L. Arurault, Y.X. Tong, J. Phys. Chem. C 113 (4) (2009) 1235–1241.
[27] X.H. Lu, X. Huang, S.L. Xie, D.Z. Zheng, Z.Q. Liu, C.L. Liang, Y.X. Tong, Langmuir 26 (10) (2010) 7569–7573.
[28] Z.L. Wang, G.R. Li, Y.N. Ou, Z.P. Feng, D.L. Qu, Y.X. Tong, J. Phys. Chem. C 115 (2) (2011) 351–356.
[29] L.S. Zivkovic, V. Lair, O. Lupan, M. Cassir, A. Ringuede, Acta Phys. Pol. 120 (2) (2011) 298–302.
[30] S. Cimino, L. Lisi, G. Totarella, S. Barison, M. Musiani, E. Verlato, J. Ind. Eng. Chem. 66 (2018) 404–410.
[31] P.H. Ho, M. Ambrosetti, G. Groppi, E. Tronconi, G. Fornasari, A. Vaccari, P. Benito, Catal. Today (2019). https://doi.org/10.1016/j.cattod.2019.02.005.
[32] I. Zhitomirsky, A. Petric, Ceram. Int. 27 (2) (2001) 149–155.
[33] E.J. Ruiz, R. Ortega-Borges, L.A. Godinez, T.W. Chapman, Y. Meas-Vong, Electrochim. Acta 52 (3) (2006) 914–920.
[34] O.S. Khalipova, V. Lair, A. Ringuede, Electrochim. Acta 116 (2014) 183–187.
[35] H. Hasannejad, T. Shahrabi, M. Jafarian, A.S. Rouhaghdam, J. Alloy. Comp. 509 (5) (2011) 1924–1930.
[36] M. Santamaria, L. Asaro, P. Bocchetta, B. Megna, F. Di Quarto, J. Electrochem. Soc. 160 (6) (2013) D212–D217.
[37] M. Santamaria, L. Asaro, P. Bocchetta, B. Megna, F. Di Quarto, ECS Electrochem. Lett. 2 (6) (2013) D29–D32.
[38] Y. Choi, E.C. Brown, S.M. Haile, W. Jung, Nanomater. Energy 23 (2016) 161–171.
[39] C.Z. Yao, Z.P. Li, B.H. Wei, J.H. Zhang, J.W. Zan, G.F. Wang, H. Li, Q.J. Gong, H.X. Ma, J. Power Sources 283 (2015) 478–483.
[40] D. Grujicic, B. Pesic, Electrochim. Acta 47 (18) (2002) 2901–2912.
[41] S. Bijani, R. Schrebler, E.A. Dalchiele, M. Gabas, L. Martinez, J.R. Ramos-Barrado, J. Phys. Chem. C 115 (43) (2011) 21373–21382.
[42] A.J. Aldykiewicz, A.J. Davenport, H.S. Isaacs, J. Electrochem. Soc. 143 (1) (1996) 147–154.
[43] Y.C. Zhou, J.A. Switzer, J. Alloy. Comp. 237 (1–2) (1996) 1–5.
[44] K. Kamada, N. Enomoto, J. Hojo, Electrochim. Acta 54 (27) (2009) 6996–7000.
[45] E.C. Brown, Ph.D thesis, Caltech, 2011.
[46] F.B. Li, R.C. Newman, G.E. Thompson, Electrochim. Acta 42 (16) (1997) 2455–2464.
[47] L. Cerovic, V. Lair, O. Lupan, M. Cassir, A. Ringuede, Chem. Phys. Lett. 494 (4–6) (2010) 237–242.
[48] L. Zivkovic, V. Lair, O. Lupan, A. Ringuede, Thin Solid Films 519 (11) (2011) 3538–3543.
[49] L. Arurault, P. Monsang, J. Salley, R.S. Bes, Thin Solid Films 466 (1–2) (2004) 75–80.
[50] P. Scherrer, Göttinger Nachrichten Gesell 2 (1918) 98.
[51] B. Bouchaud, J. Balmain, G. Bonnet, F. Pedraza, Electrochim. Acta 88 (2013) 798–806.
[52] Y. Hamlaoui, F. Pedraza, C. Remazeilles, S. Cohendoz, C. Rebere, L. Tifouti, J. Creus, Mater. Chem. Phys. 113 (2–3) (2009) 650–657.
[53] D. Plecher, R. Greff, R. Peat, L.M. Peter, J. Robinson, Instrumental Methods in Electrochemistry, first ed., Ellis Woodhead, 2001.
[54] B. Allen, F. Larry, Electrochemical Methods Fundamentals and Applications, second ed., John Wiley & Sons. Inc., 2001.
[55] G. Gunawardena, G. Hills, I. Montenegro, B. Scharifker, J. Electroanal. Chem. 138 (2) (1982) 225–239.
[56] B. Scharifker, G. Hills, Electrochim. Acta 28 (7) (1983) 879–889.
[57] P.L. Mateo, G.G. Hurtado, J.B. Vidal-Abarca, J. Phys. Chem. 81 (21) (1977)

2032–2034.
[58] Q.B. Zhang, Y.X. Hua, Phys. Chem. Chem. Phys. 16 (48) (2014) 27088–27095.
[59] S. Peulon, D. Lincot, J. Electrochem. Soc. 145 (3) (1998) 864–874.
[60] M. Nobial, O. Devos, O.R. Mattos, B. Tribollet, J. Electroanal. Chem. 600 (1) (2007) 87–94.
[61] H.L. Tuller, S.R. Bishop, Chem. Lett. 39 (12) (2010) 1226–1231.
[62] F.S. Baumann, J. Fleig, H.U. Habermeier, J. Maier, Solid State Ionics 177 (11–12) (2006) 1071–1081.
[63] R.W. Powell, R.P. Tye, M.J. Hickman, Int. J. Heat Mass Transf. 8 (5) (1965) 679–688.
[64] P.S. Manning, J.D. Sirman, R.A. DeSouza, J.A. Kilner, Solid State Ionics 100 (1–2) (1997) 1–10.
[65] W.C. Chueh, S.M. Haile, Phys. Chem. Chem. Phys. 11 (37) (2009) 8144–8148.
[66] T.S. Oh, S.M. Haile, Phys. Chem. Chem. Phys. 17 (20) (2015) 13501–13511.
[67] W.C. Chueh, Y. Hao, W. Jung, S.M. Haile, Nat. Mater. 11 (2) (2012) 155–161.